Polarization and Spatial Mode Dependent Four-wave Mixing in a 4H-Silicon Carbide Microring Resonator

Shi, Xiaodong; Fan, Weichen; Lu, Yaoqin; Hansen, Anders Kragh; Chi, Mingjun; Yi, Ailun; Ou, Xin; Rottwitt, Karsten; Ou, Haiyan

Published in:
APL Photonics

Publication date:
2021

Document Version
Peer reviewed version

Polarization and Spatial Mode Dependent Four-wave Mixing in a 4H-Silicon Carbide Microring Resonator

Xiaodong Shi,[1] Weichen Fan,[1] Yaoqin Lu,[1] Anders Kragh Hansen,[1] Mingjun Chi,[1] Ailun Yi,[2] Xin Ou,[2] Karsten Rottwitt,[1] and Haiyan Ou[1, a)]

[1)] *DTU Fotonik, Technical University of Denmark, DK-2800 Lyngby, Denmark*

[2)] *State Key Laboratory of Functional Materials for Informatics, Shanghai Institute of Microsystem and Information Technology, Chinese Academy of Sciences, Shanghai 200050, China*

(Dated: 18 June 2021)

We report four-wave mixing with different polarization and spatial modes in a single 4H-silicon carbide photonic device. Our device shows great potential to perform high-dimensional multiplexing for optical communication and high-dimensional entanglement in quantum networks. We use a polarization insensitive grating coupler and a multimode microring resonator that supports three polarization and spatial mode resonances. Finally, we show the polarization dependence of the third-order nonlinearity of 4H-silicon carbide. The measured nonlinear refractive index of the light polarized along the extraordinary axis, which is $n_{2,\mathrm{TM}} = (13.1 \pm 0.7) \times 10^{-19}$ m^2/W, is twice as large as that of the light polarized along the ordinary plane, $n_{2,\mathrm{TE}} = (7.0 \pm 0.3) \times 10^{-19}$ m^2/W, indicating that the extraordinary polarization is more efficient for nonlinear experiments in the 4H-silicon carbide integrated platforms as compared to the ordinary polarization.

I. INTRODUCTION

Four-wave mixing (FWM), a third-order nonlinear process, enables many applications in both classical optical communication and quantum communication systems, such as all-optical signal processing and correlated photon-pair generation[1,2]. In the FWM process, two pump photons annihilate, while a photon pair, a signal and an idler photon, with new wavelengths are created. If the process is seeded with a signal, then any information in the signal will be transferred to the wavelength of the idler, which is referred to wavelength conversion. The wavelength conversion is regarded as an important technique for wavelength-division multiplexing (WDM) in classical optical networks[3]. Since current optical networks have made the maximal use of the WDM, polarization-division multiplexing and space-division multiplexing are considered as important emerging strategies, for the purpose of increasing the information transmission capacity considerably[4,5]. In quantum networks, by combining the time-energy entanglement based on the spontaneous FWM with the polarization entanglement and spatial mode entanglement, individual photons are able to carry more information, so quantum entanglement with high dimensionality can be achieved for large quantum capacity[6,7]. FWM is also the fundamental mechanism for Kerr frequency combs[8]. These are very promising for applications within spectroscopy and imaging[9,10]. Orthogonal polarization pumping and spatial mode multiplexing provide ways to generate two frequency combs in a single microring resonator, relaxing the demands on the fabrication precision, as well as simplifying the experimental setup[11,12]. Thus, in this paper we research FWM based on different polarization and spatial modes in a single device.

Wide-bandgap semiconductor-based integrated nonlinear platforms have seen greatly increased interest during the past decade, including Si_3N_4, AlN, $LiNbO_3$, and silicon carbide (SiC)[13–16], because of their low two-photon absorption and subsequent free-carrier absorption, which facilitates efficient nonlinear phenomena, such as FWM and second harmonic generation. Recently, SiC has attracted a lot of interest in integrated nonlinear photonics also thanks to its high refractive index, which facilitates strong mode confinement and promotes strong nonlinear interaction[17–20]. Among the different polytypes of SiC, 4H-SiC exhibits excellent crystal quality, low material absorption, and high third-order nonlinearity. 4H-SiC is a positive uniaxial crystal, in the 6mm point group[21]. The on-axis cut of the 4H-SiC wafers is commercially available, so that the extraordinary optical axis parallel to the c axis of the crystal is perpendicular to the wafer plane. As a result, optical properties of ordinary (transverse-electric (TE)) polarized light in the 4H-SiC waveguides, aligned to the wafer plane, are different from those experienced by extraordinary (transverse-magnetic (TM)) polarized light, aligned to the extraordinary optical axis[22]. Especially, the third-order nonlinear susceptibility element along the extraordinary optical axis, $\chi^{(3)}_{3333}$, is not equal to $\chi^{(3)}_{1111}$, $\chi^{(3)}_{2222}$, or the cross terms, including $\chi^{(3)}_{1122}$, $\chi^{(3)}_{1221}$, and $\chi^{(3)}_{1212}$, within the wafer plane, resulting in polarization-dependent third-order nonlinearity in 4H-SiC[23]. For nonlinear applications and experiments, the polarization with larger nonlinear refractive index is preferred to achieve the highest efficiency. Efficient FWM and optical parametric oscillation with TE polarized light in the microring resonator, which enables significant nonlinear enhancement within a small footprint, have been demonstrated in 4H-SiC-on-insulator (SiCOI) integrated platforms[17,18], while nonlinear experiments with TM polarized light have not been reported yet.

The vertical coupling scheme using gratings to couple light from the optical fiber to the planar waveguide has shown great advantages and convenience in integrated photonics[24], since it does not require post processing after the waveguide fabrication, such as cleaving and polishing. In addition, it en-

[a)] Electronic mail: haou@fotonik.dtu.dk

ables device testing on wafer scale, benefiting large volume fabrication, and has large coupling tolerance. However, the grating couplers usually have polarization selectivity, which limits the applications requiring two orthogonal polarizations. Although the inversed taper based edge coupling enables efficient light coupling of both polarizations, it usually requires a thick buried oxide layer and a thick upcladding layer, especially for the TM mode, in order to match the mode profile of the cross section with the lensed fiber. The grating based vertical coupling is more tolerant to the surrounding layers, as the light is diffracted upwards.

In this paper, we propose a flexible polarization-insensitive 4H-SiC grating coupler, that transmits both TE and TM polarized light with a broad bandwidth. We fabricate and show the experimental characterization of the grating coupler and the multimode microring resonator with three different polarization and spatial mode resonances. We also perform FWM measurements with all three modes in the 4H-SiCOI integrated platform and extract the nonlinear refractive index, and we show experimentally the polarization-dependent third-order nonlinearity in 4H-SiC integrated platforms. Thereby, we demonstrate that the extraordinary polarization is more efficient than the ordinary polarization, which has never been experimentally demonstrated before, to the best of our knowledge.

II. DEVICE DESIGN, FABRICATION, AND CHARACTERIZATION

A. Polarization-insensitive grating coupler

To couple light with different state of polarization between an optical fiber and our integrated waveguides, we designed a polarization-insensitive grating coupler. The grating type is selected to be fully etched strip gratings, so that they can be fabricated together with other devices on the chip, and have large fabrication tolerance. The simulation was carried out using the Lumerical FDTD solutions software. The strategy of the design is that we sweep the pitch and the duty cycle of the grating structure, and find the light diffraction angle between the fiber and the chip surface, for both fundamental TE and TM modes at 1550 nm. A specific diffraction angle is selected, when the grating is able to diffract both modes, simultaneously and equivalently. The grating couplers, enabling transmission of both modes, are optimized with a pitch of 1100 nm and a duty cycle of 0.48. The simulated transmission spectra of the TE and TM modes of the grating coupler are shown in Fig. 1(a), at a diffraction angle of 74°. The maximal coupling efficiency of TE and TM modes is −5.3 dB at 1571 nm and −6.3 dB at 1536 nm, respectively. The 3 dB transmission bandwidths of TE and TM modes are 130 nm and 150 nm, respectively. From the spectrum, the grating coupler is polarization independent near 1550 nm, with a coupling efficiency of ∼ −6.4 dB.

The 4H-SiCOI integrated platform was fabricated by the ion-cut process[25]. The photonic devices were fabricated in a chip with a top 4H-SiC layer of 500 nm and a buried SiO_2 layer of 2.1 µm. First, the device pattern was defined on the resist AR-P 6200.09, through e-beam lithography. Second, the pattern was transferred to an aluminum layer as a hard mask, through the metal evaporation and lift-off processes. Third, the chip was etched by inductively coupled plasma reactive ion etching (ICP-RIE), to transfer the pattern to the 4H-SiC layer. Finally, the chip was wet oxidized to reduce the thickness of the 4H-SiC layer by 100 nm, and cladded with 2.3 µm SiO_2 afterwards, by plasma-enhanced chemical vapor deposition (PECVD). The fabricated device, with a multimode microring resonator and a bus waveguide connected to a pair of grating couplers, is shown in Fig. 2. The microring resonator will be discussed later.

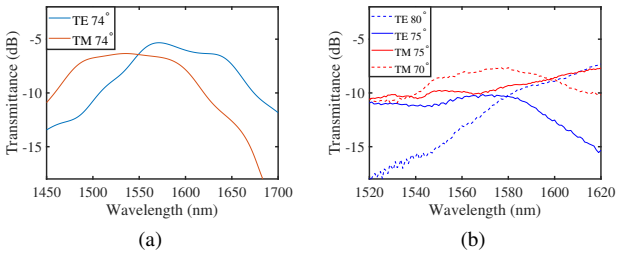

FIG. 1. (a) Simulated TE (blue) and TM (red) transmission spectra of the designed grating coupler at 74° diffraction angle. (b) Measured TE transmission spectra of the fabricated 4H-SiC grating coupler at 80° (blue dash) and 75° (blue solid) diffraction angle and TM transmission spectra at 75° (red solid) and 70° (red dash) diffraction angle.

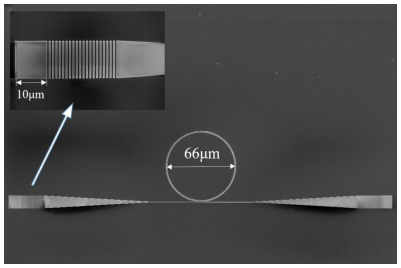

FIG. 2. Scanning electron microscope image of the microring resonator and a zoom-in image of the grating coupler.

The inset in Fig. 2 shows a zoom-in image of a fabricated grating coupler. A pair of 100 µm long tapers are used to connect the input and output grating couplers to a 500 nm wide bus waveguide, which only guides the fundamental TE and TM modes. The characterization results of the grating coupler are shown in Fig. 1(b). Due to the fabrication imperfections, the measured transmission spectra are not the same as the simulated ones. At a diffraction angle of 75°, the grating coupler is almost polarization insensitive between 1520 nm and 1580 nm, with a coupling efficiency of approximately −10.5 dB. The 3 dB transmission bandwidth of the TE and TM modes is about 80 nm and 100 nm within the measured wavelength range, respectively. It is seen from the spectrum that the peak of the TM mode transmission is beyond 1620 nm, and the maximal coupling efficiency within

the measured wavelength range is −7.8 dB. Using a higher or lower coupling angle, one can tune the peak of the transmission with a red or blue shift, respectively, and the coupling efficiency can also be changed. With a diffraction angle of 80°, the peak of the TE mode transmission is red shifted by more than 50 nm, and the maximal coupling efficiency within the measured wavelength range is increased to −7.3 dB. With a diffraction angle of 70°, the peak of the TM mode transmission is blue shifted to about 1580 nm, with a maximal coupling efficiency of −7.6 dB. However, it is also found in the experiment that the grating coupler becomes polarization dependent within the measured wavelength range, with a diffraction angle of either 70° or 80°.

B. Multimode microring resonator

The multimode microring resonator consists of a microring and a bus waveguide. The bus waveguide is 500 nm wide. The gap between the bus waveguide and the microring is 400 nm. The microring has a radius of 33 μm and a cross section of 1200 nm × 400 nm. The multimode microring resonator supports TE_{00}, TE_{10}, and TM_{00} modes, of which the distribution of the electric field is shown in the insets of Fig. 3(b), 3(c), and 3(d), respectively.

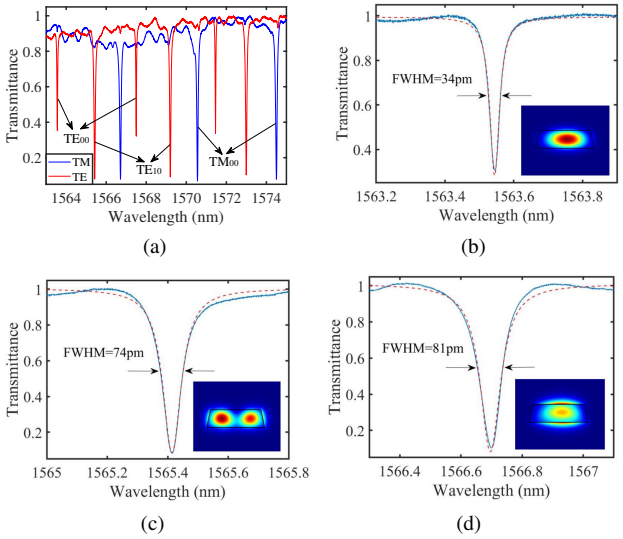

FIG. 3. (a) Measured normalized TE (red) and TM (blue) transmission spectra of the multimode 4H-SiC microring resonator. (b) (c) (d) Measured normalized transmittance (blue solid) and Lorentzian lineshape fitting spectra (red dash) of TE_{00}, TE_{10}, and TM_{00} modes, respectively, and their corresponding distribution of the electric field.

By individually launching TE and TM polarized light into the grating coupler, the normalized transmittance of TE and TM modes of the microring resonator as a function of wavelength is measured and is plotted in Fig. 3(a). Resonances for the three modes, TE_{00}, TE_{10}, and TM_{00} modes, are observed in the spectrum. The TE_{00} and TE_{10} resonances are distinguished by the difference of FSR. According to the simulation by the Lumerical MODE Solutions software, the TE_{00} mode has a smaller group index than the TE_{10} mode, so the FSR of the TE_{00} mode, equal to 482 GHz, is larger than that of the TE_{10} mode, equal to 461 GHz. The resonance of TE_{00}, TE_{10}, and TM_{00} at around 1565 nm are plotted in Fig. 3(b), 3(c), and 3(d), respectively.

The quality factor of every resonance is calculated by

$$Q = \frac{\lambda_{\text{res}}}{\lambda_{\text{FWHM}}}, \tag{1}$$

where λ_{res} is the resonant wavelength, and λ_{FWHM} is the full-width at half-maximum of the resonant transmittance. The quality factors of TE_{00}, TE_{10}, and TM_{00} modes are 46k, 21k, and 19k, respectively. The quality factor has two contributions, one from the round-trip loss in the microring resonator and the other from the coupling efficiency between the bus waveguide and the microring resonator, which are quantified by the intrinsic and external quality factors, respectively. The intrinsic (Q_{in}) and external (Q_{ex}) quality factors are expressed as[26]

$$Q_{\text{in}} = \frac{\omega}{\alpha v_g}, \tag{2}$$

and

$$Q_{\text{ex}} = \frac{\omega L}{|\kappa|^2 v_g}, \tag{3}$$

where α is the attenuation coefficient of the microring resonator, ω is the angular frequency, v_g is the group velocity, L is the circumference of the microring resonator, and κ is the coupling coefficient. From the measured transmission spectra, the intrinsic and external quality factors of all the modes are calculated, through[27]

$$\frac{1}{Q} = \frac{1}{Q_{\text{in}}} + \frac{1}{Q_{\text{ex}}}, \tag{4}$$

and

$$EX = \left| \frac{Q_{\text{in}} - Q_{\text{ex}}}{Q_{\text{in}} + Q_{\text{ex}}} \right|^2, \tag{5}$$

where EX is the extinction ratio of the resonant transmittance. By characterizing multiple microring resonators with the same width and radius, but different gaps, it is found that the microring resonator operates in the undercoupled regime for the TE_{00} mode, which indicates $Q_{\text{in}} < Q_{\text{ex}}$, and in the overcoupled regime for the TE_{10} and TM_{00} modes, which indicates $Q_{\text{in}} > Q_{\text{ex}}$. Thus, the intrinsic quality factors of TE_{00}, TE_{10}, and TM_{00} modes are calculated to be 60k, 60k, and 57k, respectively. According to Eq. 2, the propagation loss of the TE_{00}, TE_{10}, and TM_{00} modes is calculated to be 8.8 dB/cm, 9.2 dB/cm, and 9.4 dB/cm, respectively. The total propagation loss is contributed by the material absorption due to the existence of the defects, the material scattering due to the micropipe in 4H-SiC, and the waveguide confinement loss due to the scattering induced by the sidewall and surface roughness.

III. POLARIZATION AND SPATIAL MODE DEPENDENT FOUR-WAVE MIXING

A. Four-wave mixing experiment

The experimental setup used for nonlinear characterization, is shown in Fig. 4. One continuous-wave (CW) laser, used as the pump, is connected to an erbium-doped fiber amplifier (EDFA) to amplify the pump power, a tunable attenuator to vary the pump power, and a polarization controller (PC) to control the polarization of the incident light, in sequence. To monitor the pump power, a 20 dB splitter is used to separate the path into two. The other CW laser, used as the signal seed, is also connected to an EDFA and a PC. Then, the two paths are combined by a 3 dB coupler, and the light is launched into and out of the grating couplers in the 4H-SiCOI chip with the same diffraction angle of 75°. The output light is separated by another 20 dB splitter to monitor the output power and to measure the output spectrum, simultaneously.

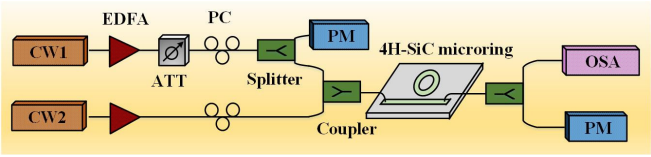

FIG. 4. Schematic experimental setup. CW: continuous-wave laser source, EDFA: erbium-doped fiber amplifier, ATT: tunable attenuator, PC: polarization controller, PM: power meter, OSA: optical spectral analyzer.

By aligning the pump and signal polarizations to be quasi-TE and sweeping them into the adjacent TE_{00} (or TE_{10}) resonances, stimulated FWM based on the TE_{00} (or TE_{10}) modes in the microring resonator is observed. Similarly, by aligning the pump and the signal polarizations to be quasi-TM and sweeping them into the adjacent TM_{00} resonances, FWM based on the TM_{00} mode in the microring resonator can be observed. In order to show FWM with sufficiently large signal to noise ratio, we performed FWM with a strong signal seed, which has the same power of 10 mW as the pump. The spectra of the strong-signal FWM based on all the three modes are shown together in Fig. 5(a). The figure shows the occurrence of three FWM processes with different polarization and spatial modes is achievable in a multimode 4H-SiC microring resonator. Two idlers of the TE_{10} and TM_{00} modes are observed on both sides of the incident light, while one idler of the TE_{00} mode cannot be distinguished due to the high amplified spontaneous emission background from the EDFA. It is noticed when the pump and signal are not on resonance, no idler can be observed from the spectrum, indicating that the FWM phenomena are not contributed by the coupled fibers, gratings, or the bus waveguide, but are only dominant by the enhancement of the multimode 4H-SiC microring resonator.

By varying the pump power, the conversion efficiency of the degenerate FWM as a function of the on-chip input pump power for the TE_{00}, TE_{10}, and TM_{00} modes are measured, as seen in Fig. 5(b). The maximal conversion efficiency, defined by the ratio of the off-resonance signal power and the on-resonance idler power, of TE_{00}, TE_{10}, and TM_{00} modes are measured to be around -47 dB, -45 dB, and -43 dB, respectively. Generally, the FWM of the TM_{00} modes has the highest conversion efficiency, while the FWM of the TE_{00} modes has the lowest conversion efficiency. It is apparent that the conversion efficiency starts to saturate above the pump power of 10 mW, approximately. Considering the bandgap of 3.26 eV for 4H-SiC, the cut-off wavelength of the two-, three-, and four-photon absorption are 760.72 nm, 1141.07 nm, and 1521.43 nm, respectively[28]. Therefore, it is not the multi-photon absorption induced nonlinear losses or subsequent free-carrier absorption that cause the conversion efficiency saturation[29]. Instead, we attribute the saturation to the absorption-induced thermal effects including the thermo-optic effect and the thermal expansion, that shift the resonance to longer wavelengths. As a result, the pump and the signal are not exactly located at the resonant wavelength of the microring resonator. In order to mitigate the thermal instability of the microring resonator, the off-chip temperature controlling by the thermoelectric cooler or the on-chip temperature controlling by the microheater can be introduced[27,30].

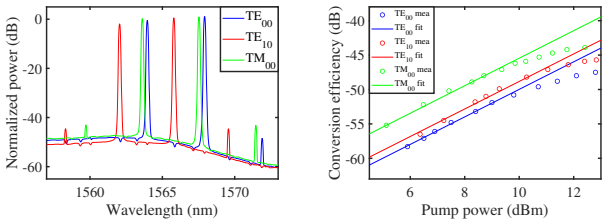

FIG. 5. (a) Measured FWM output spectra of the multimode 4H-SiC microring resonator, with TE_{00} (blue), TE_{10} (red), and TM_{00} modes (green). (b) The conversion efficiency of measured data (circle) and lines fitted to the low-power data with slope fixed at 2 (solid line) with TE_{00} (blue), TE_{10} (red), and TM_{00} (green) modes as a function of the on-chip input power in the bus waveguide.

B. Polarization dependent nonlinear refractive index

The conversion efficiency of the FWM in the microring resonators is theoretically calculated by[31]

$$CE = (\gamma P_p L_{\text{eff}})^2 F E_p^4 F E_s^2 F E_i^2, \tag{6}$$

where P_p is the pump power. In Fig. 5(b), the solid lines represents a linear fit to the data measured at low pump power with a slope of 2, which shows that the conversion efficiency of the FWM with the three modes is quadratic in the pump power, well matching Eq. 6. γ denotes the nonlinear parameter, given by

$$\gamma = \frac{2\pi n_2}{\lambda A_{\text{eff}}}, \tag{7}$$

where n_2 is the nonlinear refractive index, and A_{eff} is the effective area. The effective area of the TE_{00}, TE_{10}, and TM_{00}

modes is simulated to be 0.477 μm^2, 0.734 μm^2, and 0.790 μm^2, respectively. L_{eff} denotes the effective length, expressed as

$$L_{\text{eff}}^2 = L^2 e^{-\alpha L} \left| \frac{1 - e^{-\alpha L + j\Delta k L}}{\alpha L - j\Delta k L} \right|^2, \tag{8}$$

where $\Delta k = 2k_p - k_s - k_i$ is the phase mismatch, in which $k_{p,s,i}$ is the propagation constant of the pump, signal, and idler, respectively. The phase mismatch of TE_{00}, TE_{10}, and TM_{00} modes in the microring resonator is plotted in Fig. 6(a).

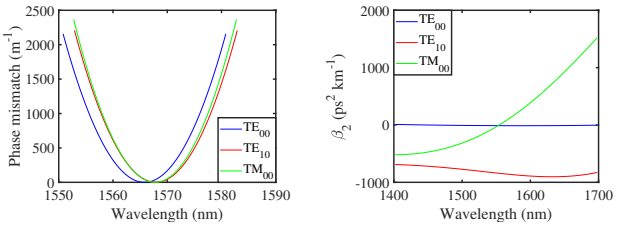

(a) (b)

FIG. 6. (a) Simulated phase mismatch of TE_{00} (blue), TE_{10} (red), and TM_{00} (green) modes as a function of the signal wavelength. (b) Simulated second-order derivative of the propagation constant of TE_{00} (blue), TE_{10} (red), and TM_{00} (green) modes as a function of the wavelength.

It is found that the phase mismatch induced effects on the effective length are very weak, as the signal and the idler are very close in wavelength to the pump. Hence, the effective lengths of TE_{00}, TE_{10}, and TM_{00} modes are calculated to be 198.85 μm, 198.44 μm, and 198.23 μm, respectively. $FE_{p,s,i}$ is the on-resonance field enhancement factor of the microring resonator for the pump, signal, and idler, respectively, which is given by

$$FE = \left| \frac{\kappa}{1 - \tau e^{-\frac{\alpha L}{2}}} \right|, \tag{9}$$

where $\tau = \sqrt{1-\kappa^2}$ is the transmission coefficients between the bus waveguide and the microring resonator, which is obtained from Eq. 3. It is found that the field enhancement factors of the pump, signal, and idler are almost equivalent for every mode. Therefore, the on-resonance field enhancement factors of TE_{00}, TE_{10}, and TM_{00} modes are calculated to be 4.0, 4.6, and 4.5, respectively. The modes with resonance approaching the critical coupling of the microring resonator, that means $Q_{in} = Q_{ex}$ and has the lowest extinction ratio in the transmittance according to Eq. 5, have the strongest enhancement. The conversion efficiency is proportional to the field enhancement factor to the power of eight, according to Eq. 6. As the field enhancement factor of the TE_{10} mode is larger than that of the TE_{00} mode, the conversion efficiency of the TE_{10} mode is higher, even though the TE_{00} mode has a larger nonlinear parameter due to its small effective area. The second-order derivative of the propagation constant of TE_{00}, TE_{10}, and TM_{00} modes is plotted in Fig. 6(b). As can be seen, the fundamental TE and TM modes have near-zero group velocity dispersion in the FWM operation wavelength range. It indicates that the resonances of the fundamental TE and TM modes are equally spaced, so the pump, signal, and idler wavelengths have tiny mismatch with the resonances. Additionally, the thickness variation of the 4H-SiC layer is below 3% within the 1 cm^2 4H-SiCOI chip, and the microring has a much smaller footprint of 3.5×10^3 μm^2, so the thickness induced dispersion variation is negligible. Based on the data of the fundamental TE and TM modes in Fig. 5(b) and Eqs. 6 - 9, the nonlinear refractive index of the ordinary and extraordinary polarized light in 4H-SiC can be extracted as $n_{2,\text{TE}} = (7.0 \pm 0.3) \times 10^{-19}$ m^2/W and $n_{2,\text{TM}} = (13.1 \pm 0.7) \times 10^{-19}$ m^2/W, respectively. The nonlinear refractive index of the TE polarized light is consistent with previous reported values[17,18], while that of the TM polarized light has not been reported yet. The high nonlinear refractive index and the strong enhancement of the TM_{00} mode makes FWM more efficient than what may be achieved using the TE_{00} or the TE_{10} modes in the experiment, resulting in the highest conversion efficiency.

The experimental results indicate that the third-order nonlinearity of 4H-SiC is polarization dependent, and the nonlinear refractive index of the extraordinary polarized light is twice as large as that of the ordinary polarized light in the 4H-SiCOI integrated platforms. The waveguide investigated in this experiment has a very thin 4H-SiC film of 400 nm, which cannot strongly confine the TM_{00} mode, as shown in the inset of Fig. 3(d). This results in a larger effective area, compared to that of the TE_{00} mode. Hence, the nonlinear parameters of the TM_{00} and TE_{00} modes are 6.66 W^{-1}m^{-1} and 5.89 W^{-1}m^{-1}, respectively, which are almost equivalent, and the higher conversion efficiency of the FWM with the TM_{00} mode is mainly contributed by the stronger field enhancement factor.

Waveguides with a thicker 4H-SiC film exhibit more similar effective areas of the TM_{00} and TE_{00} modes, so assuming the same microring resonator induced field enhancement, the nonlinear parameter of the TM_{00} mode is about twice as large as that of the TE_{00} mode according to Eq. 7, and the conversion efficiency of the FWM with TM_{00} mode is about four times as large as that of the TE_{00} mode according to Eq. 6. Therefore, TM_{00} polarization is much preferred for efficient nonlinear applications of the 4H-SiC integrated platform.

IV. CONCLUSION

In this work, we have demonstrated the design and fabrication of polarization-insensitive grating couplers with a bandwidth of over 60 nm in the 4H-SiCOI integrated platform. We have also demonstrated a multimode 4H-SiC microring resonator with three polarization and spatial mode resonances, and three FWM processes with these modes are achieved. This shows the potential of utilizing the polarization and the spatial modes as additional degrees of freedom to increase the transmission capacity of optical and quantum communication networks. We also find that the nonlinear refractive index of 4H-SiC is polarization de-

pendent, and the nonlinear refractive index of the extraordinary polarization, $n_{2,\mathrm{TM}} = (13.1 \pm 0.7) \times 10^{-19}$ m^2/W, is much stronger than that of the ordinary polarization, $n_{2,\mathrm{TE}} = (7.0 \pm 0.3) \times 10^{-19}$ m^2/W, which indicates that TM polarization is more efficient for the applications involving the third-order nonlinearity, such as Kerr-nonlinearity optical parametric oscillation and frequency comb generation.

ACKNOWLEDGMENTS

This work was supported by European Union's Horizon 2020 FET Open (SiComb, No.899679).

The data that support the findings of this study are available from the corresponding author upon reasonable request.

[1] J. Hansryd, P. A. Andrekson, M. Westlund, J. Li, and P.-O. Hedekvist, "Fiber-based optical parametric amplifiers and their applications," IEEE Journal of Selected Topics in Quantum Electronics **8**, 506–520 (2002).

[2] X. Shi, K. Guo, J. B. Christensen, M. A. U. Castaneda, X. Liu, H. Ou, and K. Rottwitt, "Multichannel photon-pair generation with strong and uniform spectral correlation in a silicon microring resonator," Physical Review Applied **12**, 034053 (2019).

[3] S. B. Yoo, "Wavelength conversion technologies for WDM network applications," Journal of Lightwave Technology **14**, 955–966 (1996).

[4] D. J. Richardson, J. M. Fini, and L. E. Nelson, "Space-division multiplexing in optical fibres," Nature Photonics **7**, 354–362 (2013).

[5] L.-W. Luo, N. Ophir, C. P. Chen, L. H. Gabrielli, C. B. Poitras, K. Bergmen, and M. Lipson, "WDM-compatible mode-division multiplexing on a silicon chip," Nature Communications **5**, 1–7 (2014).

[6] A. Orieux, M. A. Versteegh, K. D. Jöns, and S. Ducci, "Semiconductor devices for entangled photon pair generation: a review," Reports on Progress in Physics **80**, 076001 (2017).

[7] M. Kues, C. Reimer, J. M. Lukens, W. J. Munro, A. M. Weiner, D. J. Moss, and R. Morandotti, "Quantum optical microcombs," Nature Photonics **13**, 170–179 (2019).

[8] S. A. Diddams, K. Vahala, and T. Udem, "Optical frequency combs: Coherently uniting the electromagnetic spectrum," Science **369** (2020).

[9] M. Yu, Y. Okawachi, A. G. Griffith, N. Picqué, M. Lipson, and A. L. Gaeta, "Silicon-chip-based mid-infrared dual-comb spectroscopy," Nature Communications **9**, 1–6 (2018).

[10] C. Bao, M.-G. Suh, and K. Vahala, "Microresonator soliton dual-comb imaging," Optica **6**, 1110–1116 (2019).

[11] W. Wang, W. Zhang, Z. Lu, S. T. Chu, B. E. Little, Q. Yang, L. Wang, and W. Zhao, "Self-locked orthogonal polarized dual comb in a microresonator," Photonics Research **6**, 363–367 (2018).

[12] E. Lucas, G. Lihachev, R. Bouchand, N. G. Pavlov, A. S. Raja, M. Karpov, M. L. Gorodetsky, and T. J. Kippenberg, "Spatial multiplexing of soliton microcombs," Nature Photonics **12**, 699–705 (2018).

[13] M. H. P. Pfeiffer, C. Herkommer, J. Liu, T. Morais, M. Zervas, M. Geiselmann, and T. J. Kippenberg, "Photonic Damascene process for low-loss, high-confinement silicon nitride waveguides," IEEE Journal of Selected Topics in Quantum Electronics **24**, 1–11 (2018).

[14] H. Jung and H. X. Tang, "Aluminum nitride as nonlinear optical material for on-chip frequency comb generation and frequency conversion," Nanophotonics **5**, 263–271 (2016).

[15] J. Lin, F. Bo, Y. Cheng, and J. Xu, "Advances in on-chip photonic devices based on lithium niobate on insulator," Photonics Research **8**, 1910–1936 (2020).

[16] D. M. Lukin, M. A. Guidry, and J. Vučković, "Integrated quantum photonics with silicon carbide: challenges and prospects," PRX Quantum **1**, 020102 (2020).

[17] M. A. Guidry, K. Y. Yang, D. M. Lukin, A. Markosyan, J. Yang, M. M. Fejer, and J. Vučković, "Optical parametric oscillation in silicon carbide nanophotonics," Optica **7**, 1139–1142 (2020).

[18] Y. Zheng, M. Pu, A. Yi, X. Ou, and H. Ou, "4H-SiC microring resonators for nonlinear integrated photonics," Optics Letters **44**, 5784–5787 (2019).

[19] P. Xing, D. Ma, L. C. Kimerling, A. M. Agarwal, and D. T. Tan, "High efficiency four wave mixing and optical bistability in amorphous silicon carbide ring resonators," APL Photonics **5**, 076110 (2020).

[20] F. Martini and A. Politi, "Four wave mixing in 3C SiC ring resonators," Applied Physics Letters **112**, 251110 (2018).

[21] S. Wang, M. Zhan, G. Wang, H. Xuan, W. Zhang, C. Liu, C. Xu, Y. Liu, Z. Wei, and X. Chen, "4H-SiC: a new nonlinear material for midinfrared lasers," Laser & Photonics Reviews **7**, 831–838 (2013).

[22] J. Cardenas, M. Yu, Y. Okawachi, C. B. Poitras, R. K. Lau, A. Dutt, A. L. Gaeta, and M. Lipson, "Optical nonlinearities in high-confinement silicon carbide waveguides," Optics Letters **40**, 4138–4141 (2015).

[23] R. W. Boyd, *Nonlinear optics* (Academic press, 2020).

[24] R. Marchetti, C. Lacava, L. Carroll, K. Gradkowski, and P. Minzioni, "Coupling strategies for silicon photonics integrated chips," Photonics Research **7**, 201–239 (2019).

[25] A. Yi, Y. Zheng, H. Huang, J. Lin, Y. Yan, T. You, K. Huang, S. Zhang, C. Shen, M. Zhou, *et al.*, "Wafer-scale 4H-silicon carbide-on-insulator (4H–SiCOI) platform for nonlinear integrated optical devices," Optical Materials **107**, 109990 (2020).

[26] L. Guo, L. Wang, Q. Sun, M. Liu, G. Wang, W. Wang, P. Xie, W. Fan, and W. Zhao, "Mid-infrared dual-comb generation via the cross-phase modulation effect in a normal-dispersion microcavity," Applied Optics **59**, 2101–2107 (2020).

[27] K. Guo, L. Yang, X. Shi, X. Liu, Y. Cao, J. Zhang, X. Wang, J. Yang, H. Ou, and Y. Zhao, "Nonclassical optical bistability and resonance-locked regime of photon-pair sources using silicon microring resonator," Physical Review Applied **11**, 034007 (2019).

[28] H.-K. Kim, S. I. Kim, S. Kim, N.-S. Lee, H.-K. Shin, and C. W. Lee, "Relation between work function and structural properties of triangular defects in 4H-SiC epitaxial layer: Kelvin probe force microscopic and spectroscopic analyses," Nanoscale **12**, 8216–8229 (2020).

[29] J. Cardenas, S. Miller, Y. Okawachi, S. Ramelow, A. G. Griffith, A. Farsi, A. L. Gaeta, and M. Lipson, "Parametric frequency conversion in silicon carbide waveguides," in *CLEO: Science and Innovations* (Optical Society of America, 2015) pp. SF1D–7.

[30] R. Nandi, A. Goswami, and B. K. Das, "Phase controlled bistability in silicon microring resonators for nonlinear photonics," IEEE Journal of Selected Topics in Quantum Electronics **27**, 1–9 (2020).

[31] P. Absil, J. Hryniewicz, B. Little, P. Cho, R. Wilson, L. Joneckis, and P.-T. Ho, "Wavelength conversion in GaAs micro-ring resonators," Optics Letters **25**, 554–556 (2000).